Applied Surface Science 386 (2016) 393–404

Contents lists available at ScienceDirect

Applied Surface Science

journal homepage: www.elsevier.com/locate/apsusc

Magnetic Ni-Co alloys induced by water gas shift reaction, Ni-Co oxides by CO oxidation and their supercapacitor applications

Seungwon Lee[a,1], Jung-Soo Kang[b,1], Kam Tong Leung[b], Seog K. Kim[a], Youngku Sohn[a,*]

[a] Department of Chemistry, Yeungnam University, Gyeongsan, Gyeongbuk 38541, South Korea
[b] WATLab and Department of Chemistry, University of Waterloo, Waterloo, ON, N2L 3G1, Canada

ARTICLE INFO

Article history:
Received 7 January 2016
Received in revised form 3 June 2016
Accepted 9 June 2016
Available online 14 June 2016

Keywords:
Ni-Co alloy
Ni-Co oxide
Water-gas shift reaction
CO oxidation
Supercapacitor

ABSTRACT

Ni-Co alloys and oxides have attracted considerable attention in diverse fields, such as magnetic materials, energy storage and environmental/energy producing catalysts. Herein, the formation of magnetic Ni-Co alloys was induced by the water-gas shift reaction (WGSR) and the oxides were prepared by post-annealing and a CO oxidation reaction. The materials were characterized using a range of techniques. The annealed and post-CO oxidation Ni and Co-rich samples showed the crystal structures of $NiCo_2O_4(Co_3O_4)$/NiO and $NiCo_2O_4/Co_3O_4$, respectively. The Ni-Co oxides showed better supercapacitor performance than the corresponding Ni-Co alloys. The Co-rich samples exhibited better supercapacitor performance and CO oxidation activity than the Ni-rich sample. In addition, the Co-rich alloy showed a magnetization of 114 emu/g, which was approximately 2× larger than that of the Ni-rich alloy. The WGS reaction and the wide application tests are useful for designing new materials applicable to a wide range of areas.

1. Introduction

Nickel (Ni) and cobalt (Co)-based materials have been studied extensively for applications to environmental and clean energy producing catalysts, and energy storage systems [1–7]. Attempts to improve the application performance by modification of the morphology and changing the relative chemical composition with two (or more) different metals have been made. A range of morphologies have been reported [8–69], which include (porous) nanowires [8–13], mesoporous nanosheets [14–16], microspheres [17,18], nanoneedle arrays [19,20], mesoporous nanoneedles [21], nanosheets [22–28], porous nanotubes [29], yolk-shelled structures [30], flowerlike nanostructures [31–34], and nanoprisms [30] prepared using a variety methods [8–69], such as precipitation, hydrothermal/solvothermal methods, a single-spinneret electrospinning technique [29], and microwave heating approaches followed by pyrolysis [33,26]. Bimetallic mixed (or hybrid) transition metal oxides have attracted considerable attentions and been applied to CH_4/CO oxidation [35], oxygen reduction reaction [36,37], supercapacitors [9,14,15,22,34,38,39,40–43], and Li-ion batteries [2,37,44,45]. Rajeshkhanna et al. synthesized a festuca scoparia-like $Ni_{0.3}Co_{2.7}O_4$ material by precipitation followed by post-annealing, and reported a specific capacitance of 396 F/g at a current density of 1 A/g [38]. They showed that in situ grown $Ni_{0.3}Co_{2.7}O_4$ on Ni foam had a capacitance of 1423 F/g. Yuan et al. synthesized hierarchical layered $Co_{0.5}Ni_{0.5}$ hydroxides by a solvothermal method and reported a specific capacitance of 1767 F/g at a current density of 1 A/g in a 1 M KOH solution [39]. The specific capacitance was reported to be higher than those of single Co (or Ni hydroxide) and $Co_{0.5}Ni_{0.5}$ hydroxide nanosheets. Feng et al. recently summarized and discussed the applications of Ni-based materials (mainly crystal phases of hydroxides and oxides) to pseudocapacitor electrodes [6]. Zou et al. prepared $NiCo_2O_4$ micro-spheres assembled by chain-like nanowires with different exposed crystal facets, and reported that the chain-like nanowires showed higher electronic conductivity than the other mesoporous structures. They concluded that the higher electronic conductivity played a major role in the higher performance of supercapacitors [17]. The use of Ni-Co materials as a catalyst (e.g., for water splitting, steam reforming and CO oxidation) is of great interest [1,3,11,46–48,50]. Urchin-like $NiCo_2O_4$ spheres (diameters of ~6 μm) were prepared by a hydrothermal method and demonstrated as a catalyst for the oxygen reduction reaction [48]. Steam reforming of biomass was demonstrated using Ni–Co catalysts, which showed superior activity to the respective monometallic Co and Ni catalysts [11]. Wang et al. prepared $LaFeO_3$ supported Ni-

* Corresponding author.
E-mail addresses: youngkusohn@ynu.ac.kr, youngkusohn@hotmail.com (Y. Sohn).
[1] These authors equally contributed to this work

http://dx.doi.org/10.1016/j.apsusc.2016.06.050
0169-4332/

Co catalysts and reported high catalytic performance with superior anti-sintering ability [46].

Although $NiCo_2O_4$ has been studied extensively, there have been few studies on Ni (or Co-rich) Ni-Co oxides and alloys. In the present work, two different transition metals of Ni and Co were used to prepare mixed metal oxides and alloys. The application tests included CO oxidation, water-gas shift reaction, magnetism, and supercapacitor electrochemical measurements.

2. Experimental

2.1. Chemicals and the preparation of the materials

A stoichiometric amount (Co/Ni = 0.02 mol/0.02 mol and 0.027 mol/0.013 mol) of cobalt chloride hexahydrate (98%, Sigma-Aldrich) and nickel chloride hexahydrate (≥98%, Sigma-Aldrich) were dissolved completely in 40 mL of deionized water by magnetic stirring. Subsequently, 2 mL of a 1.0 M NaOH solution was added to the solution to obtain precipitates. The solution was transferred to a Teflon-lined autoclave and heated to 120 °C in an oven for 12 h. After the desired reaction time, the sample was cooled naturally to room temperature and the powder samples were collected by centrifugation followed by washing repeatedly with deionized water and ethanol. The collected samples were fully dried in an oven set to 70 °C before further characterization. The as-prepared sample was annealed thermally in a furnace at 600 °C for 3 h.

2.2. Characterization

Scanning electron microscopy (SEM, Hitachi S-4800) images were obtained at an acceleration voltage of 10 keV. Energy dispersive X-ray spectroscopy (EDS) was carried out on a Hitachi S-4200 scanning electron microscope. The crystal phases of the samples were examined by X-ray diffraction (XRD, PANalytical X' Pert Pro MPD) using Cu Kα radiation (40 kV and 30 mA). X-ray photoelectron spectroscopy (XPS, Thermo-VG Scientific K-Alpha spectrometer equipped with a hemispherical energy analyzer) was performed using a monochromated Al *K*α X-ray (E = 1486.6 eV) source. The Fourier transform infrared (FT-IR) spectra were collected using a Thermo Scientific Nicolet iS10 spectrometer in diamond attenuated total reflectance (ATR) mode. The magnetization versus applied field (M-H) profiles of the samples (after WGS reaction) were recorded using a Quantum Design MPMS SQUID magnetometer. The applied magnetic field was between −30 and 30 kOe and the temperatures were at 1.8, 5, 77, and 300 K. The temperature dependent magnetization curves were recorded in zero field cooling (ZFC) and field cooled cooling (FCC) modes.

2.3. CO oxidation and water-gas shift reactions

The CO oxidation experiments were performed using the as-prepared powder samples. 20 mg of the sample was loaded in a quartz U-tube (4 mm of inner diameter) under a CO(1.0%)/O_2 (2.5%)/N_2 atmosphere at a flow rate of 40 mL/min. The CO oxidation (or CO_2 formation) profile with temperature (heating rate of 10 °C/min) was recorded using a RGA200 mass spectrometer (Stanford Research Systems, USA). For the water-gas shift reaction (WGSR), 5% CO/N_2 gas and water vapor were introduced into the sample. The other experimental conditions were the same as the CO oxidation experiment.

2.4. Electrochemical property tests

A typical three-electrode (working, counter and reference electrodes) system was used for electrochemistry. A Pt wire and Ag/AgCl electrode were used as the counter and a reference electrodes, respectively. Three different samples were tested; thermal annealed, 2nd run CO oxidation and 2nd run WGSR samples. The preparation of a working electrode was as follows. 60% of the synthesized materials, 10% of acetylene black and 10% of poly(vinylidene fluoride) (PVDF) were dispersed and mixed in a N-methyl-2-pyrrolidone (NMP) solvent. The slurry was embedded onto a Ni foam and dried completely in an oven (70 °C). The Ni foam was finally pellet-pressed to produce the working electrode. Cyclic voltammetry (CV) and galvanic charging-discharging tests were conducted in a 6.0 M KOH aqueous solution using the three electrode cell on a CHI660D electrochemical work station (CH Instruments, USA) at room temperature. The specific capacitance (C) from the charge-discharge curves was calculated using the following equation: $C(F/g) = (I \cdot t)/(m \cdot \Delta V)$, where I is the discharge current (A), t is the time for discharge, m is the mass of the material, and ΔV is the voltage range. The electrochemical impedance was examined over the frequency range, 0.01 Hz to 0.1 MHz.

3. Results and discussion

3.1. Morphology and crystal structure

Fig. 1 shows typical SEM images (Supporting information, Fig. S1) of the as-prepared (A and B) and annealed (A_{an} and B_{an}) Ni-Co samples. Sample A was Ni-rich in synthesis while sample B was Co-rich. The morphology of sample A appeared as hexagonal plates (~500 nm) with a green color while sample B had the appearance of stacked sharp-edged rocks with a pink color (Supporting information, Fig. S2). Generally, Ni and Co complexes have green and pink colors, respectively, which is consistent with the present study [70]. Upon thermal annealing at 600 °C, both the morphology and the colors changed drastically, most likely due to their changes in crystal structure. Sample A became aggregated chain-like particles in white/gray and sample B became stacked particles (50–300 nm) with a black color. The two annealed samples were examined by EDS. Ni, Co and O were commonly found with no other impurity peaks. The Ni-rich sample, A_{an}, showed Ni (31%), Co (14%) and O (55%), while the Co-rich sample, B_{an}, showed Ni (7%), Co (31%) and O (61%).

Fig. 2 shows the X-ray diffraction (XRD) patterns of the as-prepared and annealed Ni-Co materials. For the as-prepared Ni-rich sample A, all the assigned XRD peaks were matched to those of hexagonal P-3m1 $Ni(OH)_2$ (JCPDS 1-074-2075) and/or hexagonal P-3m1 $Co(OH)_2$ (JCPDS 1-074-1057). Based on EDS (Fig. 1), the XRD result was attributed to $Ni_xCo_{1-x}(OH)_2$, where $x > 1 - x$, which is in good consistence with the literature [15,71]. Uniform mixed $Ni_xCo_{1-x}(OH)_2$ could be obtained because of the similar solubility constants of $Ni(OH)_2$ and $Co(OH)_2$ [14], via the reaction of $xNi^{2+} + (1\text{-}x)\ Co^{2+} + 2OH^- \rightarrow Ni_xCo_{1-x}(OH)_2$. Liu et al. reported that the XRD peak position was not affected significantly by the Co^{2+}/Ni^{2+} ratio, due to the similar ionic radius of the two metal ions [71]. Yuan et al. synthesized layered Co–Ni hydroxides using Co nitrate and Ni nitrate in an ethanol/water mixed solution by a hydrothermal method and evaluate the electrochemical performance [39]. Upon annealing the sample (A_{an}), the XRD patterns could be resolved into at least two crystal phases of rhombohedral R-3m NiO (JCPDS 1-089-3080) and cubic Fd-3m $NiCo_2O_4$ (JCPDS 1-073-1702) with a 66% and 34% in composition, respectively (Supporting information, Fig. S3). The XRD patterns of $NiCo_2O_4$ were also attributed to Co_3O_4 because of the similar XRD patterns. For the as-prepared Co-rich sample B, the XRD patterns matched those of rhombohedral R-3m $Co_2(OH)_3Cl$ (JCPDS 1-073-2134). Based on EDS (Fig. 1), the XRD pattern was attributed to $Ni_xCo_{1-x}(OH)_3Cl$, where $x < 1 - x$. Upon annealing the sample (B_{an}), the XRD patterns

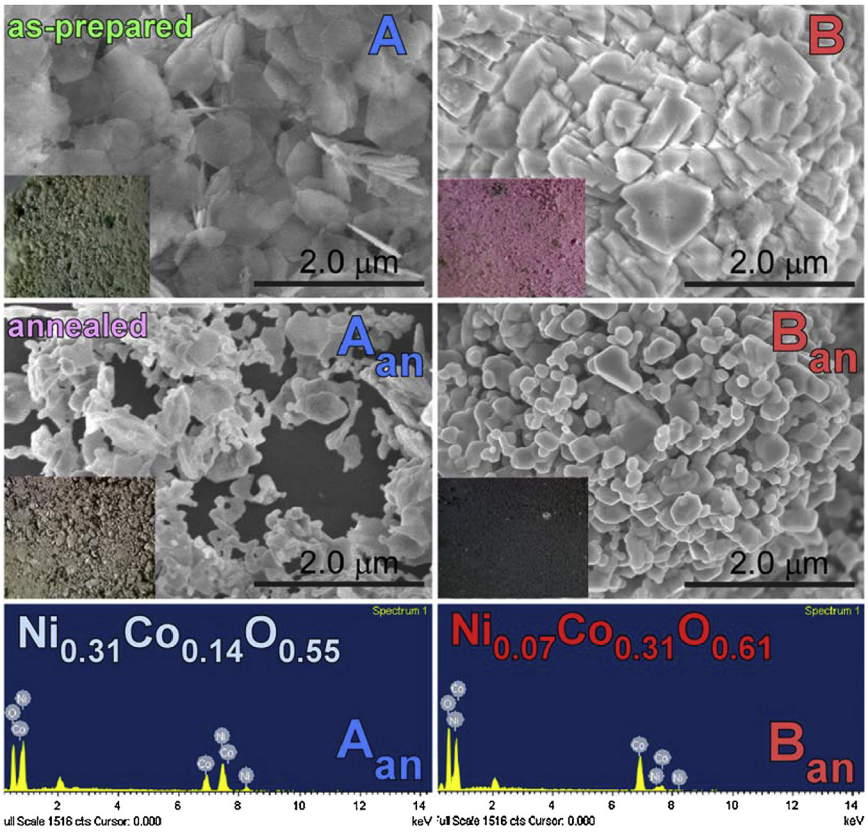

Fig. 1. SEM images of the as-prepared (A and B) and annealed (A_{an} and B_{an}) samples. EDS (bottom) of the annealed (A_{an} and B_{an}) samples. The inset photographs illustrate the colors of the corresponding powder samples.

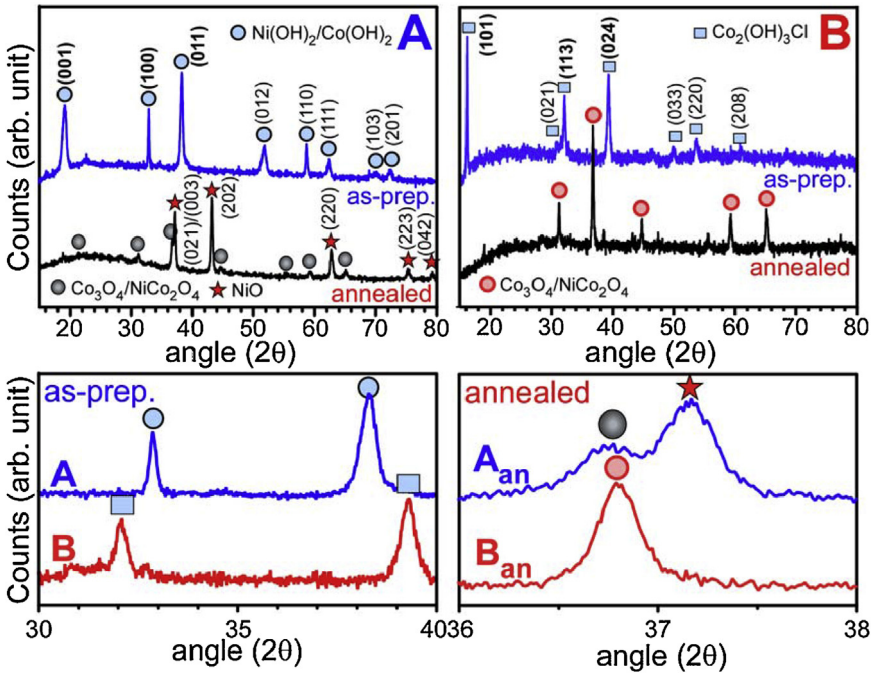

Fig. 2. Powder X-ray diffraction patterns of the as-prepared (A and B) and annealed (A_{an} and B_{an}) samples. Sample A was Ni-rich and sample B was Co-rich. The bottom XRD patterns emphasized the selected regions for the as-prepared (A and B) and annealed (A_{an} and B_{an}) samples.

were found to be $NiCo_2O_4$ (and minor Co_3O_4). Similarly, Hu et al. prepared $Ni_{1/3}Co_{2/3}(OH)_2Br_{1/3}{\cdot}nH_2O$ layered plates (in pink color) by a precipitation method using cobalt chloride, nickel chloride and hexamethylenetetramine in deionized water, and obtained $NiCo_2O_4$ platelets by post-thermal annealing [70].

The CO oxidation activity was tested for the Ni and Co-rich samples and displayed in Fig. 3. The CO oxidation study has been

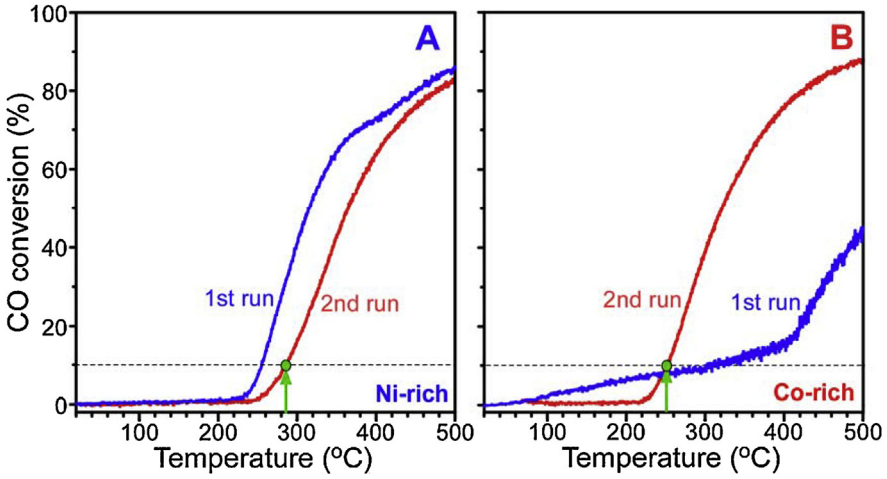

Fig. 3. Temperature programmed first and second run CO oxidation conversion (%) profiles for the Ni-rich (A) and Co-rich (B) samples. The dot lines indicate 10% CO conversion. The arrows pointing to the closed circles indicate the temperature at 10% CO conversion in the second run.

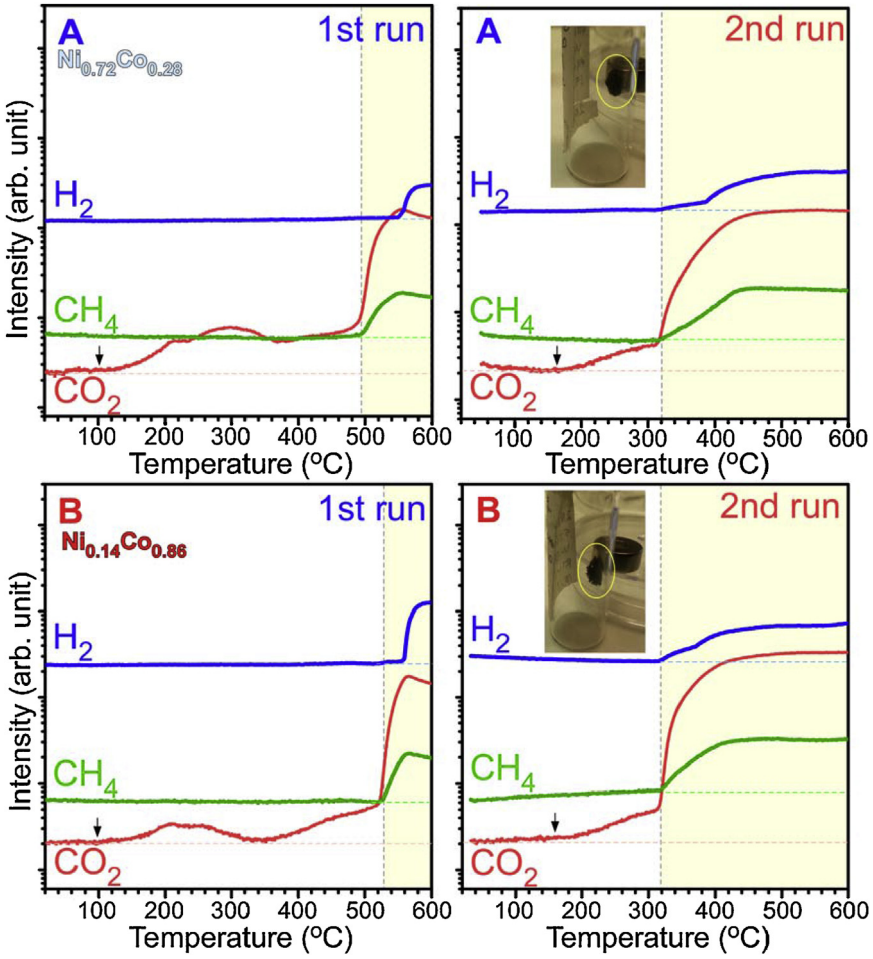

Fig. 4. First and second run WGSR mass profiles of the Ni-rich (A) and Co-rich (B) samples. The inset photographs show the magnetic properties of the corresponding powder samples after WGSR.

performed actively to achieve clean environment [48,72–79]. Pure Co_3O_4 commonly shows very low temperature CO oxidation activity, as low as −78 °C [79]. For the first run of the Ni-rich sample A, the onset of CO oxidation appeared at 230 °C and $T_{10\%}$ (the temperature at 10% CO conversion) was observed at 255 °C. In the second run, the activity was rather poor, and the onset and $T_{10\%}$ were observed at 250 °C and 285 °C, respectively. In the first run, the Ni-Co complex was unstable and thermally decomposed to more stable Ni-Co oxides. It should be emphasized here that the running temperature was below the thermal decomposition temperature of the complexes [70]. In addition, the annealed sample showed no the crystal structure of the Ni-Co complex. Therefore, the first run was the CO oxidation test for the unstable Ni-Co complex while the second run was the test for the more stable Ni-Co oxides. The crystal structure

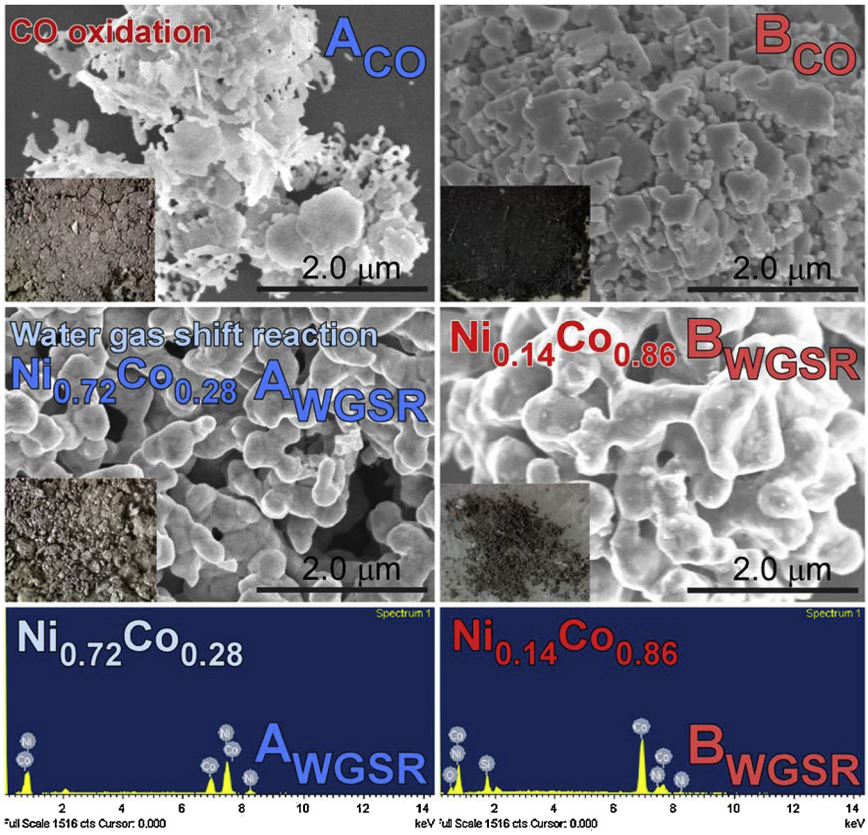

Fig. 5. SEM images of the Ni-rich and Co-rich samples after CO oxidation (top; A_{CO} and B_{CO}) and WGSR (middle; A_{WGSR} and B_{WGSR}). EDS of the Ni-rich (A_{WGSR}) and Co-rich (B_{WGSR}) samples after WGSR.

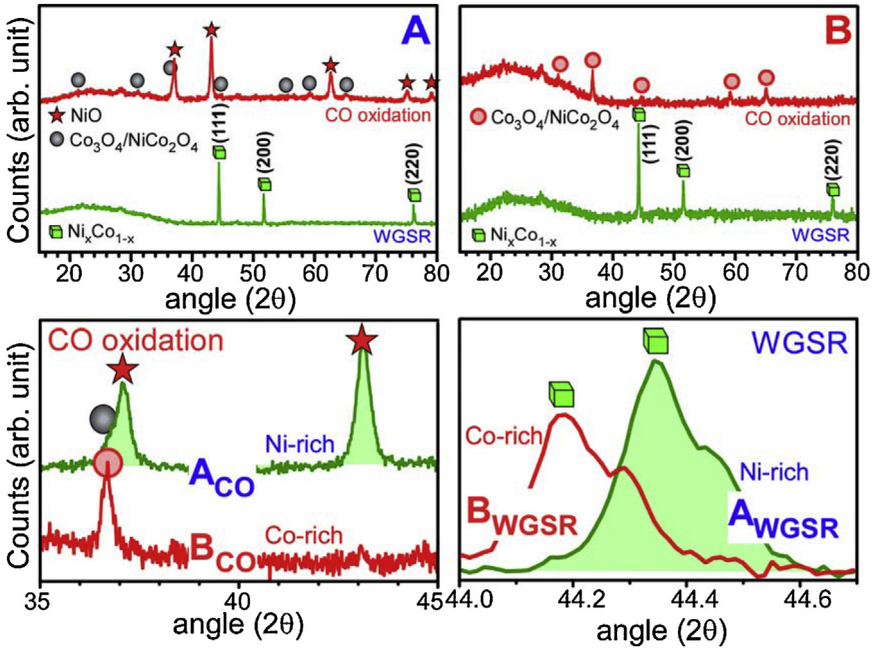

Fig. 6. Powder XRD patterns of samples A (top left) and B (top right) after CO oxidation (A_{CO} and B_{CO}) and WGSR (A_{WGSR} and B_{WGSR}). Sample A is Ni-rich and sample B is Co-rich. The bottom XRD patterns emphasize the selected regions for the samples after CO oxidation and those after WGSR.

of the stable oxides was confirmed by XRD, which will be discussed later. For the first run of the Co-rich sample B, the CO oxidation onset was observed at approximately 80 °C. In the second run, the onset was observed at 220 °C, which was 30 °C lower than that of the Ni-rich sample. $T_{10\%}$ was observed at approximately 250 °C.

The water-gas shift reaction (WGSR) has attracted considerable interest for hydrogen production [80–82]. Fig. 4 presents the WGSR profiles for the first and second run of the Ni-rich (A) and Co-rich (B) samples. Three species of CO_2, H_2 and CH_4 were commonly detected. On the other hand, CO_2 was only detected in the low tem-

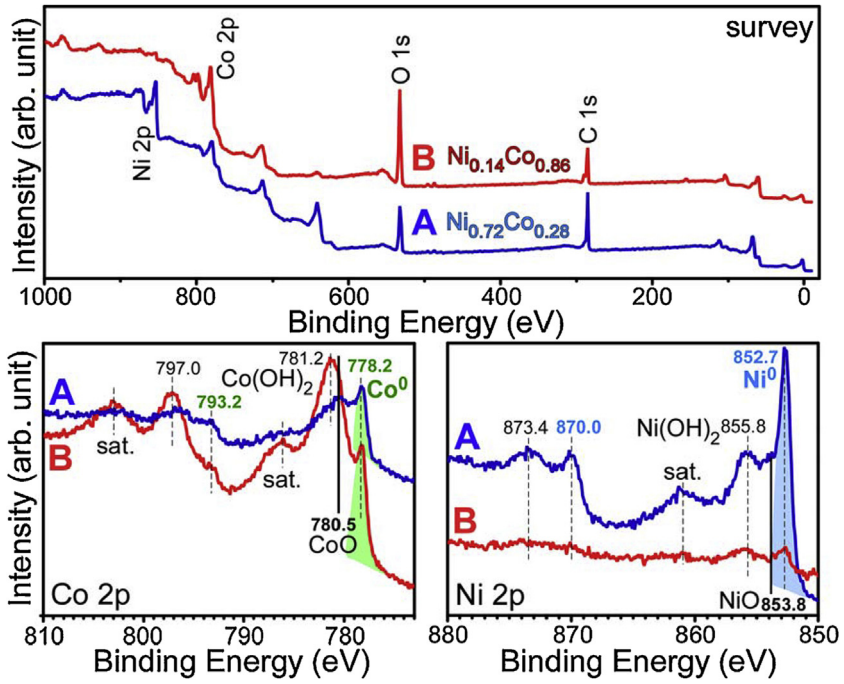

Fig. 7. Survey (top), high resolution Co 2p and Ni 2p XPS spectra of the Ni-rich (A_{WGSR}) and Co-rich (B_{WGSR}) samples after WGSR.

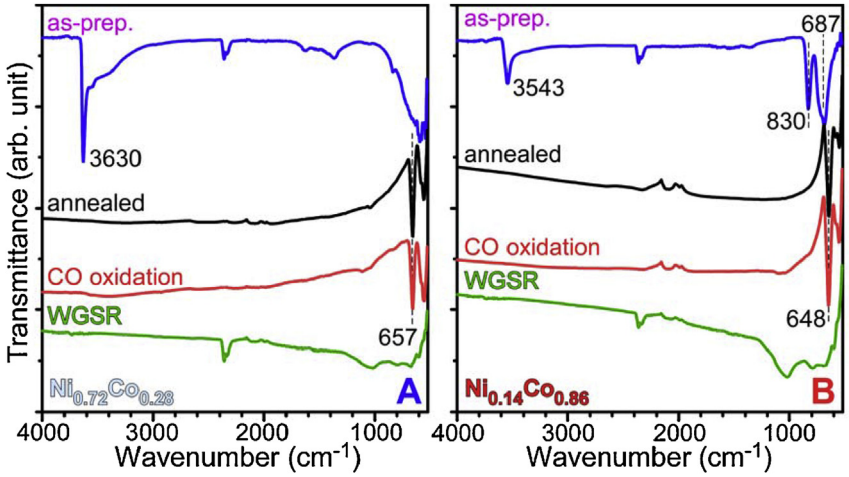

Fig. 8. FT-IR spectra of the as-prepared (A and B), annealed (A_{an} and B_{an}), post-CO oxidation (A_{CO} and B_{CO}), and post-WGSR (A_{WGSR} and B_{WGSR}) samples.

perature region while all three species were detected together in the high temperature region. In the first run, the CO_2 signal began to appear at approximately 100 °C and showed fluctuations of the intensity between 100 and 500 °C. In this region, CO reacts with the oxygen of the material to form CO_2. In addition, the unstable Ni-Co complex decomposed to form Ni-Co oxide, as discussed in Fig. 3. At 495 °C for sample A and 530 °C for sample B, abrupt increases in both CO_2 and H_2 were observed, which can be explained by the WGSR mechanism below[80–82].

$$H_2O_{ad} \rightarrow H_{ad} + OH_{ad}$$

$$CO_{ad} + OH_{ad} \rightarrow CO_2(g) + H_{ad}$$

$$H_{ad} + H_{ad} \rightarrow H_2(g)$$

CH_4 was also detected as an undesirable side product and was formed via a reaction of CO and H_2 as follows [80–82]:

$$CO + 3H_2 \rightarrow CH_4 + H_2O$$

$$CO + H_2 \rightarrow 1/2CH_4 + 1/2CO_2$$

In the second run, the CO_2 signal (or CO oxidation) began to appear at approximately 160 °C with no fluctuations. In the region between 160 °C and 320 °C, CO appears to react with surface oxygen to form CO_2. As there was no external supply of oxygen, the oxygen of the Ni-Co oxides could be consumed completely during the WGSR, as confirmed by XRD. At temperatures above 320 °C, three species were observed, which were explained using the same mechanism discussed above. The WGSR temperature in the second run was reduced dramatically by approximately 180 °C compared to the first run. The Ni and Co-rich samples showed similar catalytic activity. Before WGSR, the two samples were non-magnetic.

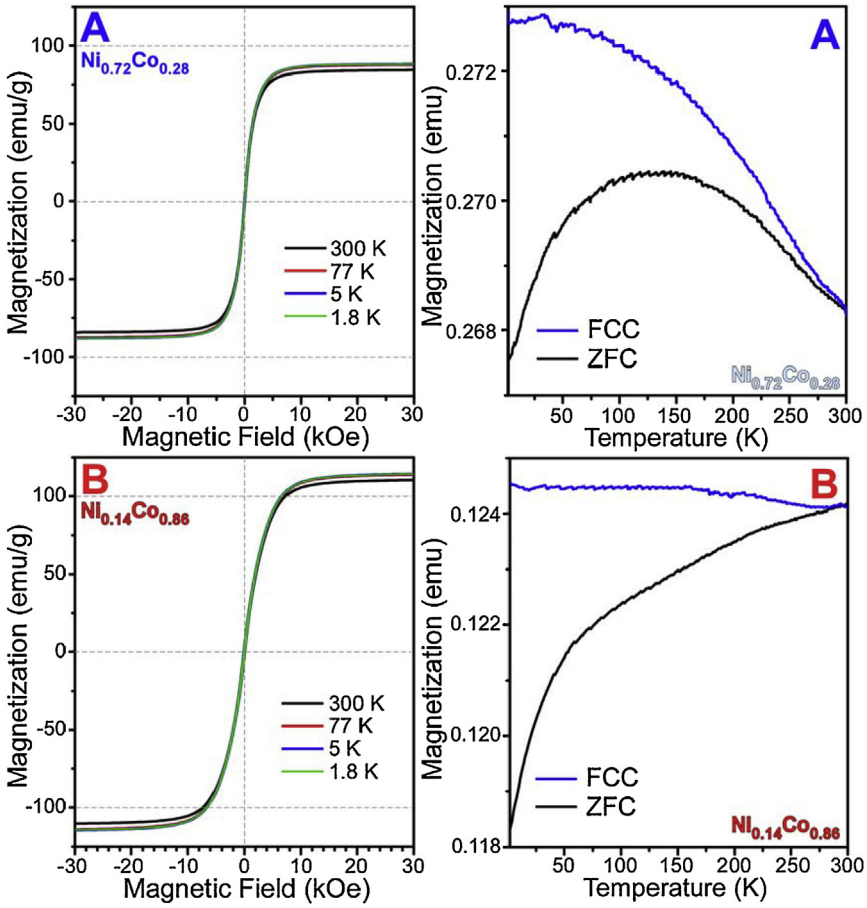

Fig. 9. Magnetization (M–H) curves (left column) at temperatures of 1.8, 5, 77, and 300 K for the samples (A and B) after WGSR. Magnetization with temperature in the FCC and ZFC modes (right column) at an applied field of 1.0 kOe.

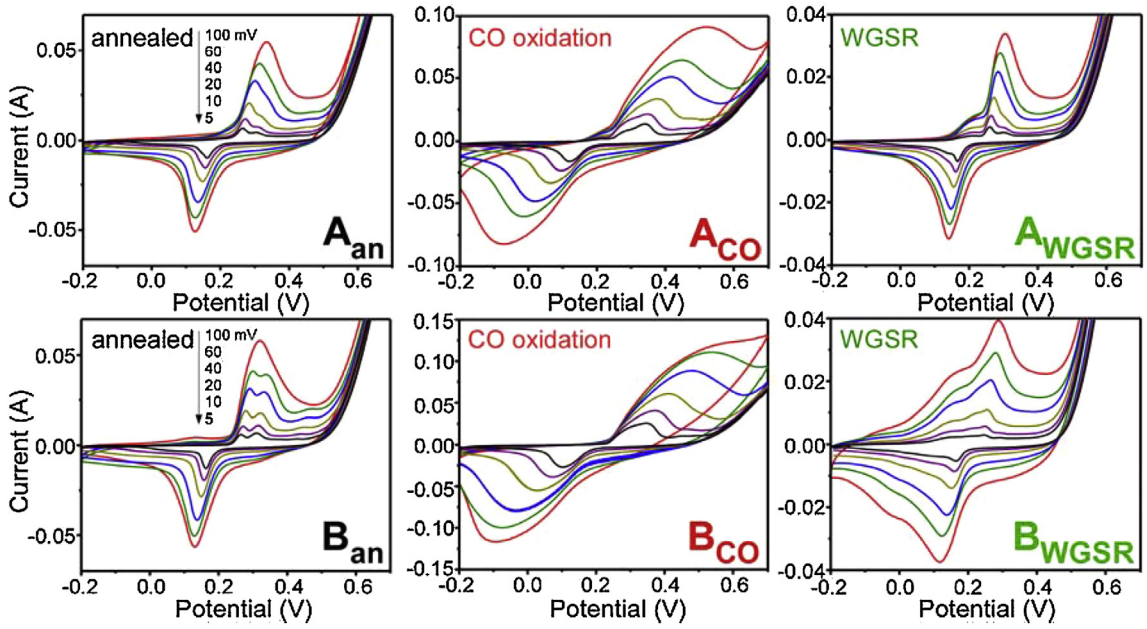

Fig. 10. CV curves (a voltage range: −0.2 V ~+0.7 V) at different scan rates (5, 10, 20, 40, 60, and 100 mV/s) of the samples after annealing (A_{an} and B_{an}), CO oxidation (A_{CO} and B_{CO}) and WGSR (A_{WGSR} and B_{WGSR}).

On the other hand, the samples became black and magnetic after the WGSR (Supporting information, Fig. S2).

Fig. 5 shows typical SEM images of the Ni-rich and Co-rich samples after the 2nd runs CO oxidation (A_{CO} and B_{CO}) and the WGSR (A_{WGSR} and B_{WGSR}). The morphology and color after CO oxida-

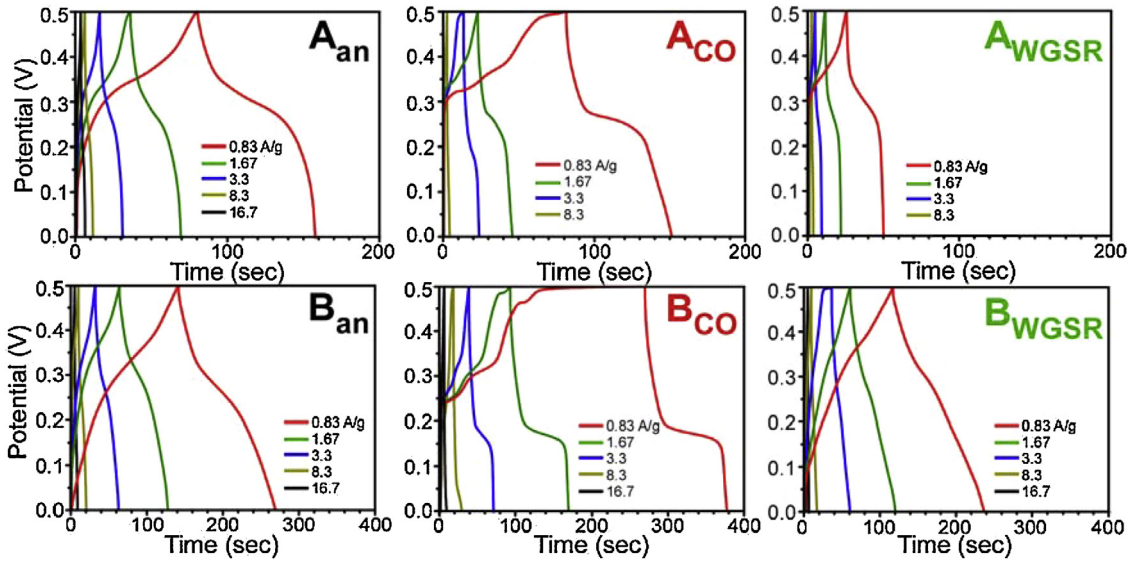

Fig. 11. Charge-discharge curves at different current densities (0.83, 1.67, 3.3, 8.3, and 16.7 A/g) of the samples after annealing (A_{an} and B_{an}), CO oxidation (A_{CO} and B_{CO}) and WGSR (A_{WGSR} and B_{WGSR}).

tion were similar to the corresponding annealed samples shown in Fig. 1. This suggests that the crystal structures of the samples after CO oxidation were similar to those of the annealed samples. Upon WGSR, the color of the sample became brighter compared to the annealed and post-CO oxidation samples, and the morphology changed to a worm-like structure with a sub-μm size. Interestingly, the oxygen intensity decreased dramatically according to EDS of the samples after WGSR. The Ni-rich sample, A_{WGSR}, showed a negligible amount of oxygen and sample B_{WGSR} showed very weak oxygen signal. The Ni/Co ratios for the A_{WGSR} and B_{WGSR} samples were estimated to be 72%/28% and 14%/86%, respectively. The oxygen of the Ni-Co oxides was consumed by CO oxidation via the reaction, CO + O_{ad} (the oxides) → CO_2(g), with no external oxygen supply.

The resulting crystal structures of the Ni-rich and Co-rich samples after the 2nd run CO oxidation (A_{CO} and B_{CO}) and WGSR (A_{WGSR} and B_{WGSR}) were examined. We assumed that the crystal structure after the 1st run was similar to that of the 2nd run because of thermal decomposition to more stable form after the 1st run. However, the crystallinity of the 2nd run sample was plausibly higher compared with that of the 1st run sample. Fig. 6 shows the corresponding powder XRD patterns. For the Ni-rich sample after CO oxidation (A_{CO}), the crystal structure was similar to that of the annealed sample, which consists mainly of NiO and $NiCo_2O_4/Co_3O_4$ but appeared to be more uniform (Supporting information, Fig. S3). For the Co-rich sample after CO oxidation (B_{CO}), the crystal structure was assigned to $NiCo_2O_4/Co_3O_4$. After the WGSR, the XRD patterns were changed dramatically. Three XRD peaks were observed between 15° and 80° 2θ, which were assigned to the (111), (200) and (220) planes of the Ni-Co alloy. The XRD peak positions of the (111) plane for the Ni-rich ($Ni_{0.72}Co_{0.28}$) and Co-rich ($Ni_{0.14}Co_{0.86}$) samples were observed at 44.36° and 44.18° 2θ, respectively.

XPS was employed to check the chemical composition of the Ni-Co alloy particles fabricated by WGSR. The survey XPS scan showed the peaks only corresponding to Co, Ni, O, and C. The Ni-rich sample A_{WGS} showed a stronger Ni 2p signal than the Co 2p signal, while the Co-rich sample B showed a stronger Co 2p signal than the Ni 2p signal. This suggests that samples A and B were Ni-rich and Co-rich samples, respectively. Although the relative intensities were different, the XPS peak positions were similar for the A_{WGSR} and B_{WGSR} samples. Because EDS and XRD showed no oxide/hydroxide states, the strong O 1s XPS peak was attributed mainly to surface states. The O 1s peaks at 529.5 and 531.8 eV were assigned to lattice oxygen and chemisorbed $OH/O^-/O_2^-$ species, respectively (Supporting information, Fig. S4) [75,77,83]. The O 1s peak at 531.8 eV for the Co-rich sample (B_{WGSR}) was stronger than that of the Ni-rich sample (A_{WGSR}). This was closely related to the stronger Co 2p XPS peak of $Co(OH)_2$ compared to the weaker Ni 2p XPS peak of $Ni(OH)_2$. For Co 2p XPS, sharp Co $2p_{3/2}$ and Co $2p_{1/2}$ XPS peaks were observed at 778.2 and 793.2 eV, respectively, and the spin-orbit (SO) splitting energy was 15.0 eV. This was attributed to metallic Co [36]. The other Co $2p_{3/2}$ XPS peaks were observed at 780.5 and 781.2 eV, which were attributed to CoO and $Co(OH)_2$, respectively. The Co $2p_{1/2}$ XPS peak of $Co(OH)_2$ was observed at 797.0 eV. The oxidation state of Co^{2+} was confirmed by the broad satellite peaks at approximately 786 and 804 eV [14,20,48,84]. Metallic Co and Ni were oxidized to form CoO and NiO on the surface, respectively, and the surface also showed metal hydroxide species. For Ni 2p XPS, two Ni $2p_{3/2}$ peaks were observed at 852.7 and 870.0 eV, with a spin-orbit splitting energy of 17.3 eV. This could be due to metallic Ni. The other small Ni $2p_{3/2}$ XPS peaks at 853.8 and 855.8 eV were attributed to NiO and $Ni(OH)_2$, respectively [20]. The corresponding Ni $2p_{1/2}$ XPS peak of $Ni(OH)_2$ was observed at 873.4 eV.

Fig. 8 displays the FT-IR spectra of the as-prepared (A and B), annealed (A_{an} and B_{an}), post-CO oxidation (A_{CO} and B_{CO}), and post-WGSR (A_{WGSR} and B_{WGSR}) samples. For the as-prepared samples A and B, the sharp peaks at 3630 (for sample A) and 3542 cm^{-1} (for sample B) were assigned to the M-OH stretching vibrations [39,84,85]. As discussed in Fig. 2, samples A and B were $Ni_xCo_{1-x}(OH)_2$ and $Ni_xCo_{1-x}(OH)_3Cl$, respectively, which contained M-OH bonds. The corresponding vibration modes were also observed between 550 and 900 cm^{-1}. No M-OH vibration modes were observed for the annealed and post-CO oxidation samples, as expected. The Ni and Co-rich samples showed metal-O vibrations for Ni-Co oxides at 657 and 648 cm^{-1}, respectively [13,27,28,84].

The magnetic properties were examined for the post-WGSR Ni (A_{WGSR}) and Co-rich samples (B_{WGSR}), whose magnetic properties were induced by WGSR [36]. As mentioned above, the Ni-Co oxides were not attracted by a magnet, but were attracted to the magnet after WGSR. Fig. 9 presents the magnetization (M) with an applied magnetic field (H) by SQUID. The magnetization according to temperature (1.8 – 300 K) was measured in field-cooled-cooling (FCC) and zero-field-cooling (ZFC) modes in a magnetic field of 1.0 kOe. The magnetic hysteresis loop was quite narrow but was

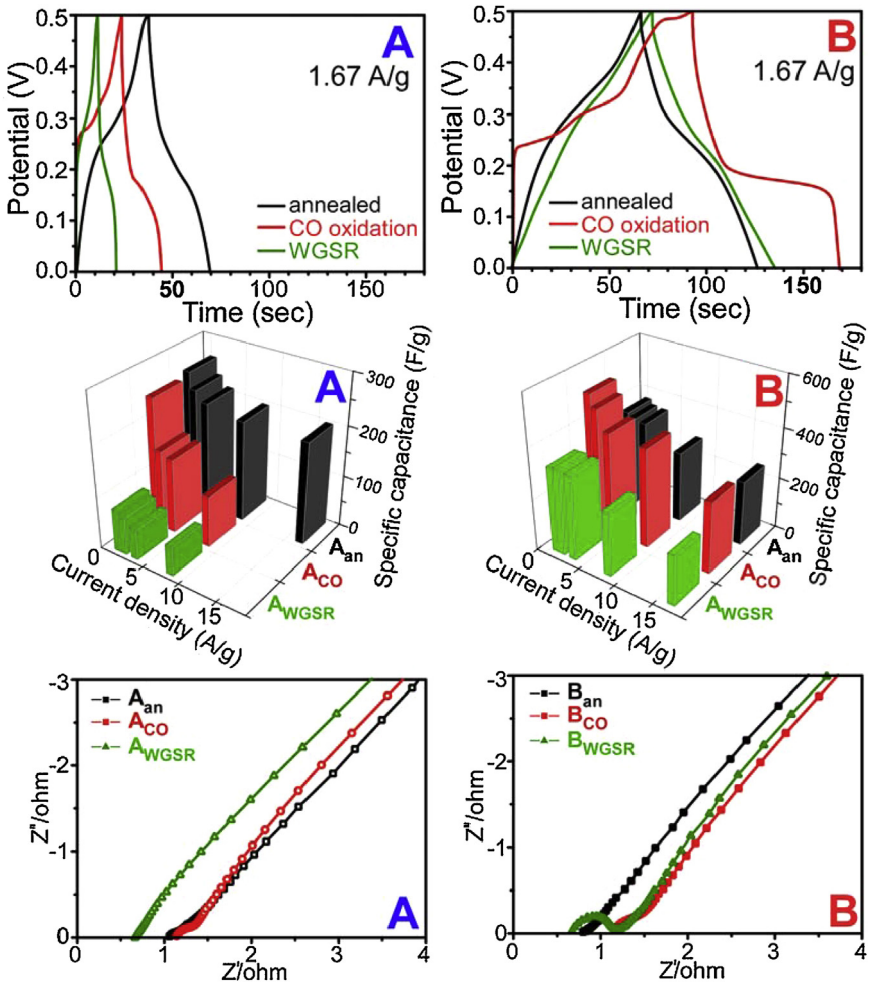

Fig. 12. Comparison of the charge-discharge curves (top) at a fixed current density of 1.67 A/g. Calculated specific capacitances (middle) and Nyquist impedance plots (bottom) for samples A and B after annealing (A_{an} and B_{an}), CO oxidation (A_{CO} and B_{CO}) and WGSR (A_{WGSR} and B_{WGSR}).

observed at a low temperature of 1.8 K, indicating ferromagnetic properties (Supporting information, Fig. S5). For the Ni-rich sample after WGSR (A_{WGSR}), the saturation magnetization values were measured to be 58 and 61 emu g^{-1} at 300 K and 1.8 K, respectively. The FCC and ZFC curves showed separation from 300 K with decreasing temperature. The FCC was increased gradually with decreasing temperature, which is related to the improvement of the magnetic alignment. On the other hand, the ZFC curve first increased and then decreased with decreasing temperature. The curve showed a broad maximum at 125K, which was related to blocking-unblocking of magnetic alignment [86]. For the Co-rich sample after WGSR ($Ni_{0.14}Co_{0.86}$), the magnetization magnitude was double that of sample A_{WGSR} ($Ni_{0.72}Co_{0.28}$), and the saturation magnetization values were measured to be 110 and 114 emu g^{-1} at 300 K and 1.8 K, respectively. The FCC and ZFC behaviors were critically different from those of the A_{WGSR} sample. The FCC curve showed an almost constant value, which was attributed to the hindrance of magnetic order and/or interparticle interactions [87]. In addition, the ZFC value showed a sharp decrease with decreasing temperature. Wei et al. reported saturation magnetization of 111.33 emu and 103.58 emu/g for flower-like $Ni_{0.48}Co_{0.52}$ alloy spheres (~800 nm) and hierarchical flower-like $Ni_{0.47}Co_{0.53}$ alloys (~5 μm), respectively [66], which is consistent with the Co-rich sample.

Fig. 10 shows the cyclic voltammetry (CV) curves, which were obtained over the potential range, −0.2 V and 0.7 V, at different scan rates of 5, 10, 20, 40, 60, and 100 mV/s. The strong reduction-oxidation (redox) peaks were observed and the redox peak positions became wider with increasing scan rates, which are characteristic of the pseudocapacitive behavior. The CV currents increased with increasing scan rate from 5 to 100 mV/s, which is an indication of a typical diffusion-controlled process. The CV curves of the samples after CO oxidation were much broader than those of the annealed sample and the sample after WGSR. For the Ni-rich sample, the areas of the CV curves were in the order of A_{WGSR} $<A_{an}<A_{Co}$, which reflected the electrochemical performance of a material [18]. The Co-rich sample B showed similar behavior. Cyclic cathodic and anodic peaks were observed due to reduction and oxidation of $Co^{2+} \leftrightarrow Co^{3+} \leftrightarrow Co^{4+}$ and $Ni^{2+} \leftrightarrow Ni^{3+}$ [19,25,20,10,12]. For the Co-rich sample, two cathodic peaks were observed and their intensities were dependent on the relative amounts of Ni and Co ions. For the Ni-rich sample, the former peak was stronger, whereas the latter peak became dominant for the Co-rich sample, which is good consistence with the literature [38].

Galvanostatic charge-discharge tests were performed to evaluate the capacitance over the potential range, 0.0–0.5 V. Fig. 11 shows the charge-discharge profiles of the Ni-rich (A) and Co-rich (B) samples after thermal annealing (A_{an} and B_{an}), CO oxidation (A_{CO} and B_{CO}) and WGSR (A_{WGSR} and B_{WGSR}). The specific capacitance (F/g) was calculated using the equation, $C_m = (I \cdot \Delta t)/(\Delta V \cdot m)$, where C_m is the specific capacitance, I is the constant discharge current (A), Δt is discharge time (sec), ΔV is the applied potential window, and m is the mass (g) of the active material [8,10,12]. The charge-discharge time (Δt) generally increased with increas-

ing current density, as expected. The charge-discharge time was strongly dependent on the sample treatment and the relative amount of Ni and Co.

Fig. 12 compares the charge-discharge time for the Ni-rich A and Co-rich B samples after annealing, CO oxidation and WGSR at a fixed current density of 1.67 A/g. The calculated specific capacitances and Nyquist plots for samples A and B are also shown. For the Ni-rich samples, the specific capacitance (or discharging time) was generally in the order of $A_{WGSR} < A_{CO} < A_{an}$. The specific capacitance of the Ni-rich samples after thermal annealing (A_{an}), CO oxidation (A_{CO}) and WGSR (A_{WGSR}) were 230, 154 and 73 F/g at a fixed current density of 1.67 A/g, respectively. The specific capacitance commonly decreased after WGSR. For the Co-rich samples, the specific capacitance was in the order of B_{WGSR} (334 F/g) $< B_{an}$ (351 F/g) $< B_{CO}$ (473 F/g) at a fixed current density. The Ni-rich sample showed poorer supercapacitive performance than the Co-rich sample. The Nyquist plot consists of imaginary (Z″) and ideal (Z′) parts. For the Ni-rich sample, the solution/charge-transfer resistance in the high frequency region was observed in the order of $A_{WGSR} < A_{CO} \approx A_{an}$. The Ni-Co alloy was more conductive after the WGSR due to the presence of metallic Ni and Co, as discussed above. The straight slope in the low frequency region represents the Warburg diffusion resistance [10,34]. For the Co-rich sample, the solution/charge-transfer resistance showed an order of $A_{an} < A_{CO} \approx A_{WGSR}$. Sample B after the WGSR showed higher resistance, possibly due to surface oxidation, as discussed in Fig. 7.

5. Conclusions

Magnetic worm-like Ni-Co alloys could be fabricated by the WGSR over Ni-Co complex and the non-magnetic Ni-Co oxides were synthesized by annealing and post-CO oxidation.

1) XRD showed that the annealed and post-CO oxidation Ni-rich samples exhibited the crystal structures of $NiCo_2O_4$(Co_3O_4)/NiO formed from the $Ni_xCo_{1-x}(OH)_2$ complex. On the other hand, the Co-rich sample showed the $NiCo_2O_4/Co_3O_4$ structure after the annealing and CO oxidation of $Ni_xCo_{1-x}(OH)_3Cl$.
2) The CO oxidation activity ($CO + 1/2O_2 \rightarrow CO_2$) for the Ni-rich and Co-rich samples was observed at 285 and 250 °C, respectively.
3) Magnetic Ni-Co alloys were formed by the complete consumption of oxygen during WGSR. This was confirmed by EDX, XRD and XPS. Only CO_2 was detected in the low temperature region, whereas CO_2, H_2 and CH_4 were observed in the high temperature region.
4) The Co-rich alloy ($Ni_{0.14}Co_{0.86}$) showed a saturation magnetization of 114 emu g^{-1} at 1.8 K, which was significantly higher than that (61 emu g^{-1} at 1.8 K) for the Ni-rich sample ($Ni_{0.72}Co_{0.28}$).
5) Ni-Co oxides showed superior supercapacitor performance to the Ni-Co alloys. The Co-rich oxides showed a specific capacitance of 471 F/g at a current density of 1.67 A/g, which was approximately 2× larger than that (230 F/g) of the Ni-rich sample.

This study further emphasized the possible applications of Ni-Co based materials to various areas of CO oxidation for a clean environment, WGSR for energy production and supercapacitor tests for energy storage. In addition, WGSR was found to be useful for the fabrication of magnetic bi-metal alloys.

Acknowledgements

This study was supported by Dong-il Culture and Scholarship Foundation research grants in 2015 and by the National Research Foundation of Korea (NRF) grant funded by the Korean government (MEST) (NRF-2014R1A1A2055923).

Appendix A. Supplementary data

Supplementary data associated with this article can be found, in the online version, at http://dx.doi.org/10.1016/j.apsusc.2016.06.050.

References

[1] P. Du, R. Eisenberg, Catalysts made of earth-abundant elements (Co, Ni, Fe) for water splitting: recent progress and future challenges, Energy Environ. Sci. 5 (2012) 6012–6021.
[2] S. Goriparti, E. Miele, F.D. Angelis, E.D. Fabrizio, R.P. Zaccaria, C. Capiglia, Review on recent progress of nanostructured anode materials for Li-ion batteries, J. Power Sources 257 (2014) 421–443.
[3] R. Subbaraman, D. Tripkovic, K.-C. Chang, D. Strmcnik, A.P. Paulikas, P. Hirunsit, M. Chan, J. Greeley, V. Stamenkovic, N.M. Markovic, Trends in activity for the water electrolyser reactions on 3d M(Ni, Co, Fe, Mn) hydr(oxy)oxide catalysts, Nature Mater. 12 (2012) 550–557.
[4] C.Z. Yuan, H.B. Wu, Y. Xie, X.W. Lou, Mixed transition metal oxides: design, controllable synthesis and energy-related applications, Angew. Chem. Int. Ed. 53 (2014) 1488–1504.
[5] D.P. Dubal, P. Gomez-Romero, B.R. Sankapal, R. Holze, Nickel cobaltite as an emerging material for supercapacitors: an overview, Nano Energy 11 (2015) 377–399.
[6] L. Feng, Y. Zhu, H. Ding, C. Ni, Recent progress in nickel based materials for high performance pseudocapacitor electrodes, J. Power Sources 267 (2014) 430–444.
[7] J. Wang, W. Cui, Q. Liu, Z. Xing, A.M. Asiri, X. Sun, Recent progress in cobalt-Based heterogeneous catalysts for electrochemical water splitting, Adv. Mater. 28 (2015) 215–230.
[8] H. Jiang, J. Ma, C. Li, Hierarchical porous $NiCo_2O_4$ nanowires for high-rate supercapacitors, Chem. Commun. 48 (2012) 4465–4467.
[9] C. Yuan, J. Li, L. Hou, L. Yang, L. Shen, X. Zhang, Facile template-free synthesis of ultralayered mesoporous nickel cobaltite nanowires towards high-performance electrochemical capacitors, J. Mater. Chem. 22 (2012) 16084–16090.
[10] F. Yang, J. Yao, F. Liu, H. He, M. Zhou, P. Xiao, Y. Zhang, Ni–Co oxides nanowire arrays grown on ordered TiO_2 nanotubes with high performance in supercapacitors, J. Mater. Chem. A 1 (2013) 594–601.
[11] L. Wang, D. Li, M. Koike, H. Watanabe, Y. Xu, Y. Nakagawa, K. Tomishige, Catalytic performance and characterization of Ni–Co catalysts for the steam reforming of biomass tar to synthesis gas, Fuel 112 (2013) 654–661.
[12] X. Liu, J. Liu, X. Sun, $NiCo_2O_4$@NiO hybrid arrays with improved electrochemical performance for pseudocapacitors, J. Mater. Chem. A 3 (2015) 13900–13905.
[13] M. Yu, J. Chen, Y. Ma, J. Zhang, J. Liu, S. Li, J. An, Hydrothermal synthesis of $NiCo_2O_4$ nanowires/nitrogen-doped graphene for high-performance supercapacitor, Appl. Surf. Sci. 314 (2014) 1000–1006.
[14] C. Yuan, J. Li, L. Hou, X. Zhang, L. Shen, X.W. Lou, Ultrathin mesoporous $NiCo_2O_4$ nanosheets on Ni foam as advanced electrodes for supercapacitors, Adv. Funct. Mater. 22 (2012) 4592–4597.
[15] J.H. Zhong, Z.L. Wang, G.R. Li, J.W. Wang, Y.N. Ou, Y.X. Tong, $Co_3O_4/Ni(OH)_2$ composite mesoporous nanosheet networks as a promising electrode for supercapacitor applications, J. Mater. Chem. 22 (2012) 5656–5665.
[16] K. Xu, R. Zou, W. Li, Y. Xue, G. Song, Q. Liu, X. Liu, J. Hu, Self-assembling hybrid NiO/Co_3O_4 ultrathin and mesoporous nanosheetsinto flower-like architectures for pseudocapacitance, J. Mater. Chem. A 1 (2013) 9107–9113.
[17] R. Zou, K. Xu, T. Wang, G. He, Q. Liu, X. Liu, Z. Zhang, J. Hu, Chain-like $NiCo_2O_4$ nanowires with different exposed reactive planes for high-performance supercapacitors, J. Mater. Chem. A 1 (2013) 8560–8566.
[18] Y. Ma, H. Jiang, Q. Liu, W. Kang, J. Shi, Rattle-type $NiCo_2O_4$ carbon composite microspheres as electrode materials for high-performance supercapacitors, New J. Chem. 39 (2015) 7495–7502.
[19] G.Q. Zhang, H.B. Wu, H.E. Hoster, M.B. Chan-Park, X.W. Lou, Single-crystalline $NiCo_2O_4$ nanoneedle arrays grown on conductive substrates as binder-free electrodes for high-performance supercapacitors, Energy Environ. Sci. 5 (2012) 9453–9456.
[20] J. Wu, R. Mi, S. Li, P. Guo, J. Mei, H. Liu, W.-M. Lau, L.-M. Liu, Hierarchical three-dimensional $NiCo_2O_4$ nanoneedle arrays supported on Ni foam for high-performance supercapacitors, RSC Adv. 5 (2015) 25304–25311.
[21] M. Yu, J. Chen, J. Liu, S. Li, Y. Ma, J. Zhang, J. An, Mesoporous $NiCo_2O_4$ nanoneedles grown on 3D graphene-nickel foam for supercapacitor and methanol electro-oxidation, Electrochim. Acta 151 (2015) 99–108.
[22] G.X. Gao, H.B. Wu, S.J. Ding, L.M. Liu, X.W. Lou, Hierarchical $NiCo_2O_4$ nanosheets grown on Ni nanofoam as high-performance electrodes for supercapacitors, Small 11 (2015) 804–808.
[23] G.X. Gao, H.B. Wu, X.W. Lou, Citrate-assisted growth of $NiCo_2O_4$ nanosheets on reduced graphene oxides for highly reversible lithium storage, Adv. Energy Mater. 4 (2014) 1400422.

[24] G. Zhang, X.W. Lou, General solution growth of mesoporous $NiCo_2O_4$ nanosheets on various conductive substrates as high-performance electrodes for supercapacitors, Adv. Mater. 25 (2013) 976–979.
[25] J. Zhou, Y. Huang, X. Cao, B. Ouyang, W. Sun, C. Tan, Y. Zhang, Q. Ma, S. Liang, Q. Yan, H. Zhang, Two-dimensional $NiCo_2O_4$ nanosheet-coated three-dimensional graphene networks for high-rate, long-cycle-life supercapacitors, Nanoscale 7 (2015) 7035–7039.
[26] S. Khalid, C. Cao, A. Ahmad, L. Wang, M. Tanveer, I. Aslam, M. Tahir, F. Idrees, Y. Zhu, Microwave assisted synthesis of mesoporous $NiCo_2O_4$ nanosheets as electrode material for advanced flexible supercapacitors, RSC Adv. 5 (2015) 33146–33154.
[27] L. Ma, X. Shen, Z. Ji, X. Cai, G. Zhu, K. Chen, Porous $NiCo_2O_4$ nanosheets/reduced graphene oxide composite: facile synthesis and excellent capacitive performance for supercapacitors, J. Colloid Interface Sci. 440 (2015) 211–218.
[28] L. Ma, X. Shen, H. Zhou, Z. Ji, K. Chen, G. Zhu, High performance supercapacitor electrode materials based on porous $NiCo_2O_4$ hexagonal nanoplates/reduced graphene oxide composites, Chem. Eng. J. 262 (2015) 980–988.
[29] L. Li, S. Peng, Y. Cheah, P. Teh, J. Wang, G. Wee, Y. Ko, C. Wong, M. Srinivasan, Electrospun porous $NiCo_2O_4$ nanotubes as advanced electrodes for electrochemical capacitors, Chem. Eur. J. 19 (2013) 5892–5898.
[30] L. Yu, B.Y. Guan, W. Xiao, X.W. Lou, Formation of yolk-shelled Ni-Co mixed oxide nanoprisms with enhanced electrochemical performance for hybrid supercapacitors and lithium ion batteries, Adv. Energy Mater. 5 (2015) 1500981.
[31] H. Chen, J. Jiang, L. Zhang, T. Qi, D. Xia, H. Wan, Facilely synthesized porous $NiCo_2O_4$ flowerlike nanostructure for high-rate supercapacitors, J. Power Sources 248 (2014) 28–36.
[32] R.K. Gupta, J. Candler, S. Palchoudhury, K. Ramasamy, B.K. Gupta, Flexible and high performance supercapacitors based on $NiCo_2O_4$ for wide temperature range applications, Sci. Rep. 5 (2015) 15265.
[33] Y. Lei, J. Li, Y. Wang, L. Gu, Y. Chang, H. Yuan, D. Xiao, Rapid microwave-Assisted green synthesis of 3D hierarchical flower-Shaped $NiCo_2O_4$ microsphere for high-performance supercapacitor, ACS Appl. Mater. Interfaces 6 (2014) 1773–1780.
[34] T. Zhu, Z.Y. Ang, G.W. Ho, Self-assembly formation of $NiCo_2O_4$ superstructures with porous architectures for electrochemical capacitors, RSC Adv. 5 (2015) 53259–53266.
[35] Z. Ren, V. Botu, S. Wang, Y. Meng, W. Song, Y. Guo, R. Ramprasad, S.L. Suib, P.-X. Gao, Monolithically integrated spinel $M_xCo_{3-x}O_4$(M = Co, Ni, Zn) nanoarray catalysts: scalable synthesis and cation manipulation for tunable low-Temperature CH_4 and CO oxidation, Angew. Chem. Int. Ed. 53 (2014) 7223–7227.
[36] Z.Q. Liu, K. Xiao, N. Li, Y.Z. Su, H.J. Wang, S. Chen, Fabrication of hierarchical flower-like super-structures consisted of porous $NiCo_2O_4$ nanosheets and their electrochemical and magnetic properties, RSC Adv. 3 (2013) 4372–4380.
[37] G.Q. Zhang, B.Y. Xia, X. Wang, X.W. Lou, Strongly coupled $NiCo_2O_4$-rGO as a methanol-tolerant electrocatalyst for oxygen reduction reaction, Adv. Mater. 26 (2014) 2408–2412.
[38] G. Rajeshkhanna, E. Umeshbabu, P. Justin, G.R. Rao, In situ fabrication of porous festuca scoparia-like $Ni_{0.3}Co_{2.7}O_4$ nanostructures on Ni-foam: an efficient electrode material for supercapacitor applications, Int. J. Hydrogen Energy 40 (2015) 12303–12314.
[39] P. Yuan, N. Zhang, D. Zhang, T. Liu, L. Chen, R. Ma, G. Qiu, X. Liu, Controllable synthesis of layered Co–Ni hydroxide hierarchical structures for high-performance hybrid supercapacitors, J. Phys. Chem. Solids 88 (2016) 8–13.
[40] L. An, Q. Ren, W. Li, K. Xu, Y. Cao, T. Ji, R. Zou, Z. Chen, J. Hu, Highly ordered mesoporous $NiCo_2O_4$ with superior pseudocapacitance performance for supercapacitors, J. Mater. Chem. A 3 (2015) 11503–11510.
[41] V.H. Nguyen, J.-J. Shim, Three-dimensional nickel foam/graphene/$NiCo_2O_4$ as highperformance electrodes for supercapacitors, J. Power Sources 273 (2015) 110–117.
[42] M. Kuang, Y.X. Zhang, T.T. Li, K.F. Li, S.M. Zhang, G. Li, W. Zhang, Tunable synthesis of hierarchical $NiCo_2O_4$ nanosheets-decorated Cu/CuOx nanowires architectures for asymmetric electrochemical capacitors, J. Power Sources 283 (2015) 270–278.
[43] T. Wang, Y. Guo, B. Zhao, S. Yu, H.-P. Yang, D. Lu, X.-Z. Fu, R. Sun, C.-P. Wong, $NiCo_2O_4$ nanosheets in-situ grown on three dimensional porous Ni film current collectors as integrated electrodes for high-performance supercapacitors, J. Power Sources 286 (2015) 371–379.
[44] L. Liu, H. Zhang, J. Yang, Y. Mu, Y. Wang, Self-assembled novel dandelion-like $NiCo_2O_4$ microspheres@nanomeshes with superior electrochemical performance for supercapacitors and lithium-ion batteries, J. Mater. Chem. A 3 (2015) 22393–22403.
[45] G.X. Gao, H.B. Wu, S.J. Ding, X.W. Lou, Preparation of carbon-Coated $NiCo_2O_4$@SnO_2 hetero-Nanostructures and their reversible lithium storage properties, Small 11 (2015) 432–436.
[46] Z. Wang, C. Wang, S. Chen, Y. Liu, Co-Ni bimetal catalyst supported on perovskite-type oxide for steam reforming of ethanol to produce hydrogen, Int. J. Hydrogen Energy 39 (2014) 5644–5652.
[47] Y. Yue, F. Liu, L. Zhao, L. Zhang, Y. Liu, Loading oxide nano sheet supported Ni-Co alloy nanoparticles on the macroporous walls of monolithic alumina and their catalytic performance for ethanol steam reforming, Int. J. Hydrogen Energy 40 (2015) 7052–7063.
[48] Z.-Q. Liu, Q.-Z. Xu, J.-Y. Wang, N. Li, S.-H. Guo, Y.-Z. Su, H.-J. Wang, J.-H. Zhang, S. Chen, Facile hydrothermal synthesis of urchin-like $NiCo_2O_4$ spheres as efficient electrocatalysts for oxygen reduction reaction, Int. J. Hydrogen Energy 38 (2013) 6657–6662.
[49] C. Xu, D. Nie, H. Chen, Y. Wang, Y. Liu, Template-free synthesis of magnetic CoNi nanoparticles via a solvothermal method, Mater. Lett. 138 (2015) 158–161.
[50] H. Wang, Y. Ma, R. Wang, J. Key, V. Linkov, S. Ji, Liquid–liquid interface-mediated room-temperature synthesis of amorphous NiCo pompoms from ultrathin nanosheets with high catalytic activity for hydrazine oxidation, Chem. Commun. 51 (2015) 3570–3573.
[51] H. Hu, B. Guan, B. Xia, X.W. Lou, Designed formation of Co_3O_4/$NiCo_2O_4$ double-shelled nanocages with enhanced pseudocapacitive and electrocatalytic Properties, J. Am. Chem. Soc. 137 (2015) 5590–5595.
[52] P. Syedvali, G. Rajeshkhanna, E. Umeshbabu, G.U. Kiran, G.R. Rao, P. Justin, In situ fabrication of graphene decorated microstructured globe artichokes of partial molar nickel cobaltite anchored on Ni foam as a high-performance supercapacitor electrode, RSC Adv. 5 (2015) 38407–38416.
[53] Q. Tang, M. Chen, L. Wang, G. Wang, A novel asymmetric supercapacitors based on binder-free carbon fiber paper@ nickel cobaltite nanowires and graphene foam electrodes, J. Power Sources 273 (2015) 654–662.
[54] I. Arief, P.K. Mukhopadhyay, Amphiphilic triblock copolymer-assisted synthesis of hierarchical NiCo nanoflowers by homogeneous nucleation in liquid polyols, J. Magn. Magn. Mater. 372 (2014) 214–223.
[55] D. Nie, C. Xu, H. Chen, Y. Wang, J. Li, Y. Liu, Chain-like CoNi alloy microstructures fabricated by a PVP-assisted solvothermal process, Mater. Lett. 131 (2014) 306–309.
[56] B. Zhao, G. Shao, B. Fan, Y. Xie, R. Zhang, Preparation and electromagnetic wave absorption of chain-like CoNi by a hydrothermal route, J. Magn. Magn. Mater. 372 (2014) 195–200.
[57] E. Umeshbabu, G. Rajeshkhanna, G.R. Rao, Urchin and sheaf-like $NiCo_2O_4$ nanostructures: synthesis and electrochemical energy storage application, Int. J. Hydrogen Energy 39 (2014) 15627–15638.
[58] M.Y. Rafique, L. Pan, W.S. Khan, M.Z. Iqbal, H. Qiu, M.H. Farooq, M. Ellahid, Z. Guo, Controlled synthesis, phase formation, growth mechanism, and magnetic properties of 3-D CoNi alloy microstructures composed of nanorods, CrystEngComm 15 (2013) 5314–5325.
[59] Y.M. Wang, X. Zhang, C.Y. Guo, Y.Q. Zhao, C.L. Xu, H.L. Li, Controllable synthesis of 3D Ni_xCo_{1-x} oxides with different morphologies for high-capacity supercapacitors, J. Mater. Chem. A 1 (2013) 13290–13300.
[60] H.B. Wu, H. Pang, X.W. Lou, Facile synthesis of mesoporous $Ni_{0.3}Co_{2.7}O_4$ hierarchical structures for high-performance supercapacitors, Energy Environ. Sci. 6 (2013) 3619–3626.
[61] M. Cheng, M. Wen, S. Zhou, Q. Wu, B. Sun, Solvothermal synthesis of NiCo alloy icosahedral nanocrystals, Inorg. Chem. 51 (2012) 1495–1500.
[62] S. Zhou, M. Wen, N. Wang, Q. Wu, Q. Wu, L. Cheng, Highly active NiCo alloy hexagonal nanoplates with crystal plane selective dehydrogenation and visible-light photocatalysis, J. Mater. Chem. 22 (2012) 16858–16864.
[63] H. Li, J. Liao, Y. Feng, S. Yu, X. Zhang, Z. Jin, Hollow CoNi alloy submicrospheres consisting of CoNi nanoplatelets: facile synthesis and magnetic properties, Mater. Lett. 67 (2012) 346–348.
[64] H. Li, J. Liao, Y. Feng, S. Yu, X. Zhang, Z. Jin, Controlled synthesis of three-dimensional CoNi microstructures composed of single crystal CoNi nanoleaves, CrystEngComm 14 (2012) 2974–2980.
[65] L.G. Vivas, M. Vazquez, J. Escrig, S. Allende, D. Altbir, D.C. Leitao, J.P. Araujo, Magnetic anisotropy in CoNi nanowire arrays: analytical calculations and experiments, Phys. Rev. B 85 (2012) 035439.
[66] X.-W. Wei, X.-M. Zhou, K.-L. Wu, Y. Chen, 3-D flower-like NiCo alloy nano/microstructures grown by a surfactant-assisted solvothermal process, CrystEngComm 13 (2011) 1328–1332.
[67] S. Pan, Z. An, J. Zhang, G. Song, Synthesis and hierarchical assembly of CoNi flowery particles, Mater. Chem. Phys. 124 (2010) 342–346.
[68] C. Xu, D. Nie, H. Chen, Y. Wang, Y. Liu, Template-free synthesis of magnetic CoNi nanoparticles via a solvothermal method, Mater. Lett. 138 (2015) 158–161.
[69] C. Xu, D. Nie, H. Chen, Y. Wang, Y. Liu, Solvothermal synthesis of cauliflower-like CoNi microstructures with enhanced magnetic property, Mater. Lett. 142 (2015) 246–249.
[70] L. Hu, L. Wu, M. Liao, X. Hu, X. Fang, Electrical transport properties of large, individual $NiCo_2O_4$ nanoplates, Adv. Funct. Mater. 22 (2012) 998–1004.
[71] X. Liu, J. Huang, X. Wei, C. Yuan, T. Liu, D. Cao, J. Yin, G. Wang, Preparation and electrochemical performances of nanostructured $Co_xNi_{1-x}(OH)_2$ composites for supercapacitors, J. Power Sources 240 (2013) 338–343.
[72] Y. Park, S.K. Kim, D. Pradhan, Y. Sohn, Thermal H_2-treatment effects on CO/CO_2 conversion over Pd-doped CeO_2 comparison with Au and Ag-doped CeO_2, React. Kinet. Mech. Catal. 113 (2014) 85–100.
[73] S.W. Lee, S.K. Park, B.K. Min, J.G. Kang, Y. Sohn, Structural/spectroscopic analyses and H_2/O_2/CO responses of thulium (III) oxide nanosquare sheets, Appl. Surf. Sci. 307 (2014) 736–743.
[74] Y. Na, S.W. Lee, N. Roy, D. Pradhan, Y. Sohn, Room temperature light-induced recrystallization of Cu_2O cubes to CuO nanostructures in water, CrystEngComm 16 (2014) 8546–8554.
[75] W.J. Kim, D. Pradhan, Y. Sohn, Fundamental nature and CO oxidation activities of indium oxide nanostructures: 1D-wires, 2D-plates, and 3D-cubes and donuts, J. Mater. Chem. A 1 (2013) 10193–10202.

[76] W.J. Kim, S.W. Lee, Y. Sohn, Metallic Sn spheres and SnO_2@ C core-shells by anaerobic and aerobic catalytic ethanol and CO oxidation reactions over SnO_2 nanoparticles, Sci. Rep. 5 (2015) 13448.
[77] Y. Park, S.K. Kim, D. Pradhan, Y. Sohn, Surface treatment effects on CO oxidation reactions over Co Cu, and Ni-doped and codoped CeO_2 catalysts, Chem. Eng. J. 250 (2014) 25–34.
[78] Y. Sohn, SiO_2 nanospheres modified by Ag nanoparticles: surface charging and CO oxidation activity, J. Mol. Catal. A. 379 (2013) 59–67.
[79] X. Xie, Y. Li, Z.-Q. Liu, M. Haruta, W. Shen, Low-temperature oxidation of CO catalysed by Co_3O_4 nanorods, Nature 458 (2009) 746–749.
[80] E.T. Saw, U. Oemar, X.R. Tan, Y. Dub, A. Borgna, K. Hidajat, S. Kawi, Bimetallic Ni–Cu catalyst supported on CeO_2 for high-temperature water?gas shift reaction: methane suppression via enhanced CO adsorption, J. Catal. 314 (2014) 32–46.
[81] D.-W. Lee, M.S. Lee, J.Y. Lee, S. Kim, H.-J. Eom, D.J. Moon, K.-Y. Lee, The review of Cr-free Fe-based catalysts for high-temperature water-gas shift reactions, Catal. Today 210 (2013) 2–9.
[82] D.-W. Jeong, A. Jha, W.-J. Jang, W.-B. Han, H.-S. Roh, Performance of spinel ferrite catalysts integrated with mesoporous Al_2O_3 in the high temperature water–gas shift reaction, Chem. Eng. J. 265 (2015) 100–109.
[83] J.S. Gwag, Y. Sohn, Interfacial natures and controlling morphology of Co oxide nanocrystal structures by adding spectator Ni ions, Bull. Korean Chem. Soc. 33 (2012) 505–510.
[84] L. Jiang, R. Zou, W. Li, J. Sun, X. Hu, Y. Xue, G. He, J. Hu, $Ni(OH)_2$/CoO/reduced graphene oxide composites with excellent electrochemical properties, J. Mater. Chem. A 1 (2013) 478–481.
[85] B. Wang, Q. Liu, Z. Qian, X. Zhang, J. Wang, Z. Li, H. Yan, Z. Gao, F. Zhao, L. Liu, Two steps in situ structure fabrication of Ni-Al layered double hydroxide on Ni foam and its electrochemical performance for supercapacitors, J. Power Sources 246 (2014) 747–753.
[86] E. Chelebaeva, L. Raehm, J.-O. Durand, Y. Guari, J. Larionova, C. Guerin, A. Trifonov, M. Willinger, K. Thangavel, A. Lascialfari, O. Mongin, Y. Mir, M. Blanchard-Desce, Mesoporous silica nanoparticles combining two-photon excited fluorescence and magnetic properties, J. Mater. Chem. 20 (2010) 1877–1884.
[87] B. Molina-Concha, R.D. Zysler, H. Romero, Anomalous magnetization enhancement and frustration in the internal magnetic order on $(Fe_{0.69}Co_{0.31})B_{0.4}$ nanoparticles, Appl. Sci. 2 (2012) 315–326.